

Abelian topological order of $\nu = 2/5$ and $3/7$ fractional quantum Hall states in lattice models

Bartholomew Andrews, Madhav Mohan, and Titus Neupert

Department of Physics, University of Zurich, Winterthurerstrasse 190, 8057 Zurich, Switzerland

(Dated: October 26, 2021)

The observed filling factors in the fractional quantum Hall effect are, in many cases, successfully supported by established theories, such as composite fermion theory and conformal field theory, which routinely show agreement for discerning properties such as the topological indices and ground-state overlaps. There are, however, several important cases where the theories themselves disagree, which leaves verification in experiment ambiguous. One such example is the statistics of the elementary excitations supported by the ground state at $\nu = 2/5$ filling, where composite fermion theory predicts an Abelian Jain state, whereas conformal field theory predicts a non-Abelian Gaffnian. In a recent paper [Yang et al., PRB **100**, 245303 (2019)] it is argued that this discrepancy is due to implicit assumptions of short-range interactions in the composite fermion approach. We complement this work by numerically investigating the contested ground-state statistics for the $\nu = 2/5$ and $3/7$ states in the Hofstadter model. For this, we perform many-body simulations using the infinite density matrix renormalization group to compute the area law of entanglement for varying interaction range. From a detailed analysis of the topological entanglement entropies, we confirm the effective Abelian statistics for these states in the case of short-range interactions, and we quantify the onset of non-Abelian topological order. We demonstrate that not only the contested states at $\nu = 2/5$ and $3/7$, but also the Laughlin filling factors, show an increase in topological entanglement entropy as the interaction range is increased.

I. INTRODUCTION

Despite the illustrious history of the fractional quantum Hall (FQH) effect, surprisingly little is understood about the elementary excitations above the ground state in many common FQH states. Even the $\nu = 2/5$ state, the second most prominent FQH plateau, has two candidate theories with fundamentally different properties¹, which provides strong motivation for further study. One of the defining features for FQH phases of matter are their fractional excitations of the ground state, known as anyons, which can obey either Abelian or non-Abelian statistics^{2–6}. In the Abelian case, exchange of quasiparticles in a given ground state comes with a fractional phase shift of the wavefunction represented by a one-dimensional braid group, whereas in the non-Abelian case, the ground state is highly degenerate and an exchange of quasiparticles additionally shifts between ground states, which is represented by a higher-dimensional braid group. Although both experimental and theoretical investigations into Abelian states are more accessible, recent interest lies squarely on non-Abelian states due to their potential application to topological quantum computing⁷, as well as other exotic properties⁸.

The disparate state of research on the ground-state statistics of FQH states can be largely attributed to the way in which the field developed. Following the original paper by Laughlin⁹, Haldane famously proposed a hierarchy of filling fractions where the quasiparticles of the Laughlin state could themselves form FQH states ad infinitum¹⁰. Jain’s subsequent reinterpretation of the FQH effect in terms of composite fermions – one electron attached to multiple vortices – then allowed us to under-

stand the FQH plateaus in terms of the integer quantum Hall effect and derive an extended hierarchy¹¹. In both of these cases, there is no reason to suggest that FQH states at these filling fractions would yield fundamentally different quasiparticle excitations to the Laughlin state. However, when Moore and Read later studied the effective field theory of a quantum Hall liquid in their seminal paper, they predicted that the $\nu = (2+1)/2$ Pfaffian can host non-Abelian excitations⁵. A slew of similar states encompassed by the Haldane pseudopotential formalism soon followed, such as the $\nu = 2/5$ Gaffnian¹² and $\nu = 1/3$ Haffnian^{13,14}. While showing remarkable agreement with the Abelian theories in many ways, such as wavefunction overlap and topological indices, the conformal field theory (CFT) approach often fundamentally disagrees on the statistics of the elementary excitations¹.

In this paper, we investigate the cases where the two approaches disagree using large-scale numerical calculations of a microscopic Hamiltonian. In particular, we follow up the recent paper by Yang et al.¹, where it is claimed that the discrepancy between the statistics of the Abelian Jain state and non-Abelian Gaffnian at $\nu = 2/5$ filling is due to implicit assumptions of short-range interactions in the composite fermion approach. Inspired by this we investigate the ground-state quasiparticle statistics of the $\nu = 2/5$ state as we tune the interaction range, as well as another contested state at $\nu = 3/7$ ^{1,15} – mentioned in the future work section of their paper, but never previously studied. To this end, we construct detailed plots of the area law of entanglement and extrapolate to the thermodynamic limit to read off the topological entanglement entropy – an indicator of quasiparticle statistics. In agreement with their hypothesis, we confirm the effective Abelian nature of the these states when particle

interactions are short range, and we provide evidence to support the onset of non-Abelian order as the interaction range is increased. Moreover, we show that even the Laughlin filling factors can potentially host non-Abelian order if the interaction range is sufficiently large.

This paper is structured as follows. In Sec. II we introduce and justify the kinetic and interaction terms of the Hamiltonian. In Sec. III we outline the numerical method and discuss efforts to minimize the errors in our extrapolation, which is crucial for this investigation. In Sec. IV we present the results for the $\nu = 1/3, 2/5$, and $3/7$ states, and finally in Sec. V, we discuss the results with respect to the two theories and highlight promising directions for future research.

II. MODEL

In this section, we introduce the single-particle Hamiltonian in Sec. II A and the corresponding many-body Hamiltonian in Sec. II B.

A. Single-particle Hamiltonian

We consider spinless fermions hopping on a square lattice in the xy -plane subject to a perpendicular magnetic field. The single-particle Hamiltonian describing the kinetic energy is given by the Hofstadter model¹⁶

$$H_0 = \sum_{\langle ij \rangle_1} \left[t e^{i\theta_{ij}} c_i^\dagger c_j + \text{H.c.} \right], \quad (1)$$

where t is the hopping amplitude, $e^{i\theta_{ij}}$ is the Peierls phase factor, $c^\dagger(c)$ are the creation(annihilation) operators for spinless fermions, and $\langle ij \rangle_{\kappa'}$ denotes pairs of κ' 'th nearest-neighbor sites on the square lattice.

Due to the presence of the perpendicular magnetic field, $\mathbf{B} = B\hat{\mathbf{e}}_z$, the fermions acquire an Aharonov-Bohm phase as they hop around a plaquette¹⁷. The precise value of the phase along a particular path is dependent on the gauge, since $\theta_{ij} = \int_i^j \mathbf{A} \cdot d\mathbf{l}$, where \mathbf{A} is the vector potential and $d\mathbf{l}$ is the infinitesimal line element from sites i to j ¹⁸. In this paper, we choose to work in x -direction Landau gauge such that $\mathbf{A} = Bx\hat{\mathbf{e}}_y$. For this choice of gauge, the fermions only acquire a phase when they hop in the x -direction. The periodicity of the phases in the x -direction define the magnetic translation algebra¹⁹ and the unit cell of the system is extended to a magnetic unit cell (MUC) of area $A_{\text{MUC}} = q \times 1$, where q is an integer and the lattice constant, $a \equiv 1$. The dimensions of our system are $L_x \times L_y$ and, unless explicitly stated, are given in units of the corresponding MUC dimensions. Crucially, there are two competing area scales in the model, the irreducible area of a flux quantum and the magnetic unit cell area, which give rise to a fractal energy spectrum with an infinite selection of Chern bands²⁰. This frustration is typically quantified using the

flux density, defined as $n_\phi = B A_{\text{MUC}} / \phi_0 \equiv p/q$, where $\phi_0 = h/e$ is the flux quantum and p, q are coprime integers. In the square-lattice Hofstadter model, q directly corresponds to the number of bands in the spectrum and increasing q decreases the band width, such that $n_\phi \rightarrow 0$ corresponds to the continuum limit²¹. Moreover the filling factor of the lowest band is given as $\nu = n/n_\phi$, where n is the filling factor of the system.

There are several important advantages of using the Hofstadter model for this investigation. First, due to the fractal energy spectrum with any desired Chern band, the system is highly configurable and we can easily access all of the desired topological flat bands. Second, the Hamiltonian is computationally minimal, since it only requires nearest-neighbor hopping on a square lattice with a phase factor, albeit with an enlarged effective unit cell. Third, and crucially for this paper, we can tune the relevant length scale in the problem, the magnetic length, simply by adjusting the flux density. This allows us to access a larger selection of system sizes at a low computational cost. We can also choose the magnetic unit cell dimensions to be in the preferred direction for our algorithm, which in our case is the x -direction (as discussed later). This powerful combination of configurability and simplicity make the Hofstadter model an ideal choice for our study.

We note that since the kinetic energy of the system is quenched for fractional quantum Hall states, it is typically the interaction Hamiltonian that dominates the physics. Ideally, the role of the single-particle Hamiltonian is simply to facilitate tuning to the correct system configurations.

B. Many-body Hamiltonian

The many-body Hamiltonian comprises the single-particle Hamiltonian (1) with the addition of a density-density interaction term, such that

$$H(\kappa) = H_0 + \sum_{\kappa'=1}^{\kappa} V(\kappa') \sum_{\langle ij \rangle_{\kappa'}} \rho_i \rho_j, \quad (2)$$

where κ is the range of nearest neighbors summed over in the interaction term, $\rho_i = c_i^\dagger c_i$ is the fermionic density operator, and $V(\kappa') = V_0/\kappa'$ is the Coulomb potential with $V_0 = 10$. The interaction strength constant, V_0 , is chosen such that it is large compared to the band width in all cases. The form of the interaction term is chosen predominantly due to its simplicity, and hence low computational expense. Although non-Abelian FQH states were originally introduced via many-body interaction terms, it has since been shown that equivalent phases may also be stabilized with two-body interactions²²⁻²⁴.

III. METHOD

To solve the many-body problem, we employ the infinite density matrix renormalization group (iDMRG) method on a thin cylinder geometry^{25–27}. The iDMRG algorithm works by transcribing an initial wavefunction into a matrix product state (MPS) and the corresponding Hamiltonian into a matrix product operator (MPO). In traditional MPS-based DMRG, there is a matrix assigned to each site of a one-dimensional chain. In this case, since we are modeling two dimensions, the chain snakes to cover the entire system. At each site the matrices representing the wavefunction are truncated up to a MPS bond dimension, χ , such that $|\psi\rangle = \sum_{\alpha=1}^{\chi} \Lambda_{\alpha} |\alpha_L\rangle \otimes |\alpha_R\rangle$, where we perform a Schmidt decomposition such that the cylinder is spatially cut into left and right halves. Λ_{α} are referred to as the Schmidt coefficients and $|\alpha_{L/R}\rangle$ are the left/right Schmidt states. The crucial property for DMRG is that the Schmidt eigenbasis may be directly related to the eigenbasis of the reduced density matrix $\rho_{\alpha}^{L/R} = \text{Tr}_{R/L} \rho_{\alpha}$, and hence provides a way of accessing entanglement properties. In fact the Schmidt states correspond directly to the eigenstates of the reduced density matrix and the Schmidt values are the square of the eigenvalues. One of the central quantities for the algorithm is the entanglement entropy and spectrum, since this offers insight into topological features. Typically, the von Neumann entanglement entropy is used, defined as $S_{VN} = -\sum_{\alpha=1}^{\chi} \Lambda_{\alpha}^2 \ln(\Lambda_{\alpha}^2)$ with $\Lambda_{\alpha} \equiv e^{-\epsilon_{\alpha}/2}$, where ϵ_{α} are the entanglement energies. The iDMRG algorithm in this paper is set on an infinite cylinder geometry, where translational invariance is assumed along the cylinder axis (x -direction) and periodic boundary conditions are taken along the circumference (y -direction). The algorithm sweeps iteratively along the one-dimensional chain, performing two-site updates after relaxing the system in accordance with the Lanczos algorithm and truncating in accordance with the maximum given MPS bond dimension. It continues in this fashion until convergence of the energy, entropy, and other discerning quantities.

For the purposes of this project, the iDMRG algorithm offers both notable advantages, as well as some drawbacks. One of the main advantages is the semi-thermodynamic limit, meaning that a thermodynamic limit ansatz is taken along the cylinder axis. Furthermore, the system sizes attainable along the circumference are highly competitive with alternative algorithms. An added benefit is that, unlike exact diagonalization, no band project needs to be taken for the interaction Hamiltonian. This means that higher Landau level effects are taken into account. The major disadvantage of the algorithm is that it is inherently one-dimensional, which means that even modest interaction ranges on the two-dimension surface correspond to exponentially long-range interactions on the unraveled one-dimensional chain. This is particularly an issue for this project as we seek to increase the interaction range as far as possible. Nevertheless, we overcome this barrier through the use

of an optimal sampling algorithm, as explained in later sections.

The way in which we distinguish between Abelian and non-Abelian order in this paper is based on the area law of entanglement, $S = \alpha L - \gamma + O(e^{-L})$, where α is a non-universal constant dependent on the microscopic parameters of the Hamiltonian, L is the system size in a given direction, and γ is the topological entanglement entropy^{28,29}. The topological entanglement entropy cannot be removed by reducing the system size and depends inherently on the type of quasiparticle excitations hosted by the ground state. It is generally written as $\gamma = \ln(\mathcal{D})$, where $\mathcal{D} = \sqrt{\sum_a d_a}$ is the total quantum dimension of the field theory description and d_a is the quantum dimension of a quasiparticle of type a . The quantum dimension for Abelian anyons is always one, whereas for non-Abelian anyons $d_a > 1$ ²⁸. The simplest example is the $\nu = 1/3$ fermionic Laughlin state where there are three Abelian anyons of charge $e/3$, and hence the topological entanglement entropy is $\gamma = \ln(\sqrt{3})$. In general, for Abelian states at filling $\nu = r/s$ the topological entanglement entropy is given as $\gamma = \ln(\sqrt{s})$ ³⁰. For non-Abelian order, this value is larger. Hence by precisely extrapolating the value of the topological entanglement entropy from the area law of entanglement, we are able to discern whether a state exhibits Abelian or non-Abelian order.

Although the premise is simple, the execution is fraught with potential problems. The first and perhaps most apparent problem is the precision to which we are able to extrapolate to the topological entanglement entropy. In many-body numerics, such as iDMRG, we are restricted to relatively small system sizes. Not only is the area law technically non-linear at small system sizes, but more importantly, finite-size effects exist on top of this, leaving the area law data highly spread and unreliable. Second the individual data points are computed at a finite bond dimension, which may be significantly off from the actual value in the $\chi \rightarrow \infty$ limit. Even slight errors in the individual data points can have a compound effect on the total error of the topological entanglement entropy, particularly if the points are close together on the L -axis. While attempting to alleviate these issues, there is additionally an arbitrariness in how to construct the line of best fit – which points should be included and which should be left out? Minor changes in acceptance criteria can have a drastic impact on the slope and y -intercept of the linear regression. Although a lot has been achieved with such computations in the past few years^{31–33}, we argue that more precise numerics are required to draw definite and reliable conclusions. Specifically, in order to perform a stand-alone computation of the topological entanglement entropy, more care is required to address numerical and statistical errors.

In this paper, we address these issues and present a systematic method that is reliable enough to accurately compute the topological entanglement entropies for the $\nu = 1/3$ and $2/5$ states. Moreover, based on this procedure, we also obtain an estimate for the topological en-

tanglement entropy of the $\nu = 3/7$ state. First, we plot the area law of entanglement in units of magnetic length, which in the square-lattice Hofstadter model depends on the flux density through $L_y/l_B = \sqrt{2\pi n_\phi} L_y$. Since the processing cost for convergence for iDMRG scales exponentially with L_y , exploiting the natural length scale of the Hofstadter model allows us to obtain a larger number of data points at relatively low computational cost³². Second, to remove arbitrariness and optimize the flux densities considered, we choose values guided by an algorithm (Sec. A 1). For each data point, we scale the computation of the entanglement entropy with bond dimension to obtain an extrapolation with error in the $\chi \rightarrow \infty$ limit. We accept data points only if the error is smaller than 0.1% (Sec. A 2). Finally, to mitigate finite-size effects, we construct multiple lines of best fit as we incrementally exclude data in ascending L_y/l_B , and stop as soon as the linear regression of the remaining points yields $R^2 > 0.99$. This is a necessary compromise between a precisely straight line and a maximal data set (Sec. A 3). The details of the numerical method are discussed in Appendix A.

IV. RESULTS

In this section we present our results from the many-body numerical calculations. In Sec. IV A we confirm the effective Abelian statistics of FQH states with short-range interactions, and in Sec. IV B we investigate the onset of non-Abelian order as the interaction range is increased.

A. Nearest-neighbor interactions

To begin, we consider the FQH states stabilized by nearest-neighbor interactions, as defined in the interaction Hamiltonian (2) with $\kappa = 1$.

To benchmark our results, we start with the Laughlin filling $\nu = 1/3$. Although this state has been previously investigated using an area law constructed from a many-body simulation^{31–33}, we emphasize that the cited investigations are not systematic enough to be transferable for higher-order states in the hierarchy. We therefore present the computation of the $\nu = 1/3$ area law plot using our systematic procedure in Fig. 1.(a). We have algorithmically chosen our data points to avoid selection bias, we have scaled each data point with χ to eliminate convergence error, and we have systematically excluded small- L_y/l_B data to alleviate finite-size effects. Most importantly, all points are converged in the entanglement entropy to $\delta S < 0.1\%$, have a spacing of $\Delta(L_y/l_B) > 0.1$, and the linear regression satisfies $R^2 > 0.99$ (see Appendix A). Further tightening the constraints of the algorithm yields eight such points, shown in the figure. We note that for the $\nu = 1/3$ state we obtained significantly more data points that satisfy all of the criteria, which is

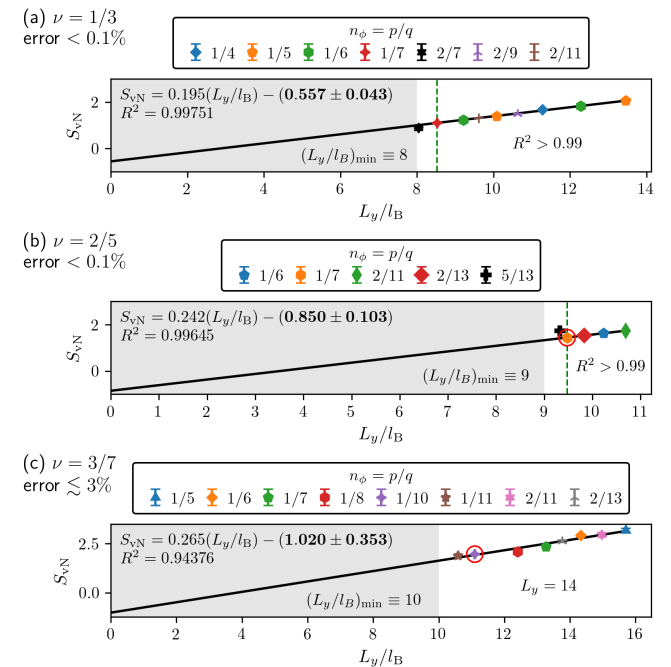


FIG. 1. Von Neumann entanglement entropy, S_{vN} , against cylinder circumference, L_y , in units of magnetic length, $l_B = (2\pi n_\phi)^{-1/2}$, for the fermionic hierarchy states at (a) $\nu = 1/3$, (b) $\nu = 2/5$, and (c) $\nu = 3/7$. In each case, we use nearest-neighbor interactions ($\kappa = 1$). (a, b) The threshold where the R^2 value first exceeds 0.99 is marked with a green dashed line. All of the points above this threshold are used to construct the line of best fit. In (c), we present the complete data set with our largest system size $L_y = 14$. In all cases, we obtain points based on the systematic procedure outlined in Appendix A with $\chi_{\max} = 3000$. The complete data sets are shown in Fig. 5 and the points circled in red are studied in Fig. 2.

why we further restricted the algorithm to yield a smaller representative sample (as detailed in Appendix B). The topological entanglement entropy obtained from these data is $\gamma = 0.557 \pm 0.043$, which agrees closely with the Abelian theory value of $\gamma = \ln(\sqrt{3}) \approx 0.549$ as expected.

We progress from the Laughlin state to the next filling in the hierarchy: $\nu = 2/5$. We hold the $\nu = 2/5$ data to the same stringent quality standards that we enforced for the $\nu = 1/3$ state. The data obtained are shown in Fig. 1.(b), which serves as our first original result. Since for the $\nu = 2/5$ state it is more difficult to satisfy configuration constraints and convergence at accessible χ , this filling presented a significant computational challenge compared to the Laughlin state³⁴. Nevertheless, we obtained a set of four data points that satisfy all of the criteria. The topological entanglement entropy obtained from these data is $\gamma = 0.850 \pm 0.103$, which agrees with the Abelian theory value of $\gamma = \ln(\sqrt{5}) \approx 0.805$ and iDMRG computations using the ground-state wavefunctions³⁰. Moreover, it is well-separated from the non-Abelian (Gaffnian) prediction of $\gamma = \ln(\sqrt{5}(\varphi^2 + 1)) \approx$

1.448, where φ is the golden ratio^{30,35}. There are several additional remarks that can be made, specifically in comparison to the Laughlin state. First, the minimum L_y/l_B to effectively eliminate finite-size effects is larger for the $\nu = 2/5$ state than for 1/3, increasing from 8.5 to 9.5. Second, the average spacing of the data on the L_y/l_B -axis is reduced. States with a larger cylinder circumference are generally more expensive to converge, and so we were not able to access high- L_y/l_B states with such stringent precision. Finally, although this figure shows all of the data points obtained in accordance to the algorithm, we generally obtained a vast set of data that corroborate this conclusion, as shown in Appendix B. The Appendix also explains how one may haphazardly reach the same conclusion when not following a rigorous procedure.

The last filling factor that we consider is the $\nu = 3/7$ state, where, unlike in the previous cases, the area law has not been previously investigated in any form. As before, we systematically select flux densities guided by our algorithm and we scale each configuration with χ so that we can extrapolate to the $\chi \rightarrow \infty$ limit. Due to computational expense of the $\nu = 3/7$ configurations, we are not able to converge every data point to within $< 0.1\%$ error and so we cannot directly use the R^2 value as an indicator of finite-size effects. Instead, we present the data for the largest system sizes that we examined ($L_y/l_B > 10$ and $L_y = 14$) with $\lesssim 3\%$ error in Fig. 1.(c). The full data set is shown in Appendix B. Interestingly, we note that there are two types of finite-size effects in the problem. Not only is there a finite-size effect due to the cylinder circumference in units of magnetic length, the physical length scale in the system, but there is also a finite-size effect due to the cylinder circumference alone, the numerical length scale. Although a large L_y/l_B value ensures that each FQH droplet has a large allocated area, a large L_y additionally ensures that there are enough sites (matrices in the MPS) in the finite direction of the algorithm to accurately represent the ground-state wavefunction. Since an increase in L_y/l_B coarsely corresponds to an increase in L_y , this is an effect that was not apparent in the previous two states. In line with the observed trend, we obtain a topological entanglement entropy of $\gamma = 1.020 \pm 0.353$, which is in agreement with the Abelian theory value of $\gamma = \ln(\sqrt{7}) \approx 0.973$, and well-separated from the non-Abelian prediction of $\gamma = \ln(\sqrt{7}(\varphi^2 + 1)) \approx 1.616$ ^{15,35}. The derivation of the total quantum dimensions is discussed in Appendix C.

To confirm the FQH nature of the configurations, we additionally examine each data point in detail. In this paper, we present the case studies for the red-circled points in Fig. 1. We start by examining the details of the $\nu = 2/5$ configuration at $n_\phi = 1/7$ and $(L_x, L_y) = (1, 10)$, shown in Fig. 2.(a-d), and subsequently the $\nu = 3/7$ configuration at $n_\phi = 1/10$ and $(L_x, L_y) = (1, 14)$, shown in Fig. 2.(e-h).

In Fig. 2.(a), we present the charge pumping of the $\nu = 2/5$ configuration as a flux is adiabatically inserted through the cylinder. This flux insertion exposes the Hall

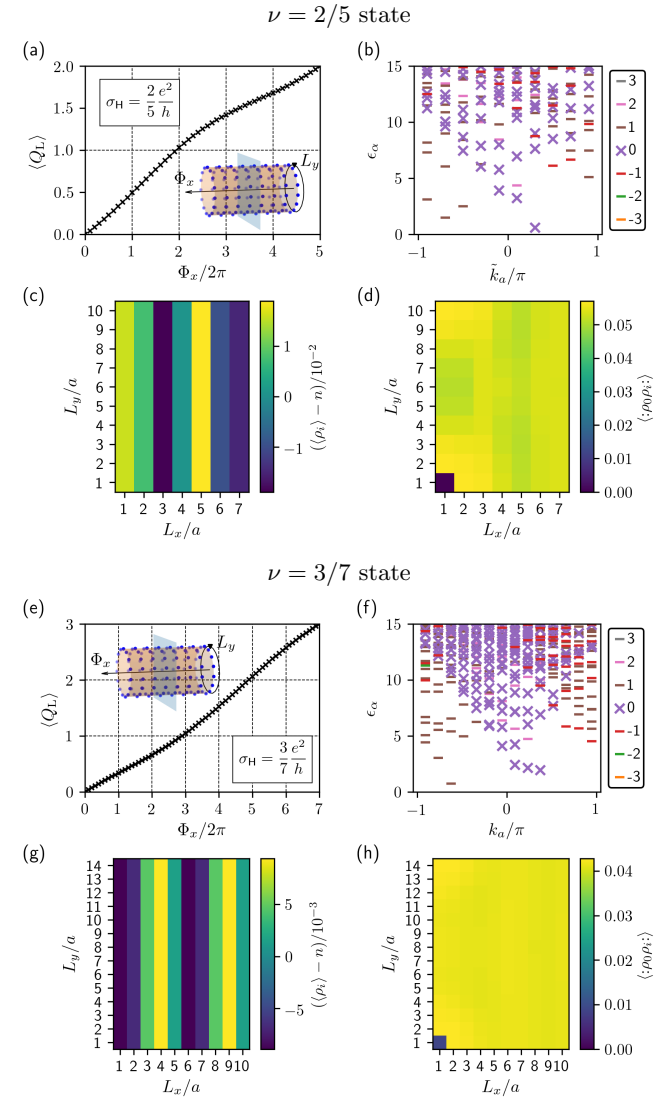


FIG. 2. Case studies of the points circled in red from Fig. 1. The $\nu = 2/5$ state is obtained at $n_\phi = 1/7$, $(L_x, L_y) = (1, 10)$, and $\chi = 800$. The $\nu = 3/7$ state is obtained at $n_\phi = 1/10$, $(L_x, L_y) = (1, 14)$, and $\chi = 2000$. (a, e) Average charge on the left half of the cylinder, $\langle Q_L \rangle$, as a function of the external flux, Φ_x , adiabatically inserted along the cylinder axis, as shown in the inset (not to scale). The charge pumping was performed at the reduced bond dimensions of $\chi = 400$ and 500, respectively. (b, f) Momentum-resolved entanglement spectrum, showing the entanglement energies, ϵ_α , as a function of the eigenvalues corresponding to the translation of Schmidt states around the cylinder, k_a , additionally colored according to their $U(1)$ charge sector. In (b) we shift the spectrum to emphasize the edge modes, such that $\tilde{k}_a/\pi \equiv [(k_a/\pi + 1) + k_0/\pi] \bmod 2 - 1$ with $k_0 = 2\pi/5$. (c, g) Average density, $\langle \rho_i \rangle$, and (d, h) two-point correlation function, $\langle \rho_0 \rho_i \rangle$, for each site in the MPS unit cell. Note that the dimensions of the MPS unit cell are given in units of the lattice constant in the figure.

conductivity, $\sigma_H = (e^2/h)C\nu$, where e is the electronic charge, h is Planck's constant, and C is the Chern number. Since we are partially filling a band of unit Chern number, the Hall conductivity is directly proportional to the filling factor. The charge pumping shows that two charges are pumped across the cut after an insertion of five flux quanta, which confirms the $\nu = 2/5$ FQH state. In Fig. 2.(b), we present the momentum-resolved entanglement spectrum obtained by rotating the cylinder around its axis. The entanglement energies are additionally labeled by their charge sector eigenvalue, corresponding to the $U(1)$ symmetry of the Hamiltonian. Using the low-lying energies in the spectrum, we can verify the counting of the edge states to be $1, 1, 2, (3), \dots$, in agreement with the Abelian CFT³⁶ and not the Gaffnian counting, which is $1, 1, 3, 5, \dots$ in the corresponding topological sector^{37,38}. We note that verification to higher order is not possible at this modest cylinder circumference. Finally, in Fig. 2.(c,d) we plot the density, $\langle \rho_i \rangle$, and two-particle correlation function, $\langle : \rho_0 \rho_i : \rangle$, respectively. The density plot shows that we are in a striped phase and the two-point correlation function has the expected form for a conventional FQH state^{21,32,39}. Most significantly, we can see from the asymmetric density and slight interference in the correlation function profile that, despite our best efforts, some minor finite-size effects still remain.

In Fig. 2.(e), we present the analogous charge pumping curve for the $\nu = 3/7$ configuration. In this case, we observe three charges pumped after an insertion of seven flux quanta, again in agreement with the expected Hall conductivity for the $\nu = 3/7$ FQH state in a $C = 1$ band. In Fig. 2.(f), we show the momentum-resolved entanglement spectrum, now at the higher resolution of $L_y = 14$. As before, we observe an edge state counting of $1, 1, 2, (3), \dots$ corresponding to an Abelian CFT. Reassuringly, the density and two-point correction function profiles in Fig. 2.(g,h) show less influence of the finite system size than the $\nu = 2/5$ configuration. The FQH configuration is again in a striped phase.

B. Tuning interaction range

Having confirmed the Abelian topological order of the $\nu = 1/3, 2/5$, and $3/7$ states when stabilized by a nearest-neighbor density-density interaction term, we now investigate the effect of increasing the interaction range, such that $\kappa \in [1, 2, 3]$.

As before, we start with the most prominent $\nu = 1/3$ state. In order to investigate the effect of tuning interaction range, we take the eight accepted points in Fig. 1.(a). Subsequently, we construct equivalent area law plots for up to second and third nearest-neighbor interactions, as shown in Fig. 3.(a). Perhaps surprisingly, our results tentatively suggest that even for the Laughlin state, the topological entanglement entropy increases as we tune the interaction range. Specifically, we notice a potential increase from $\gamma_{\kappa=1} = 0.557 \pm 0.043$ to

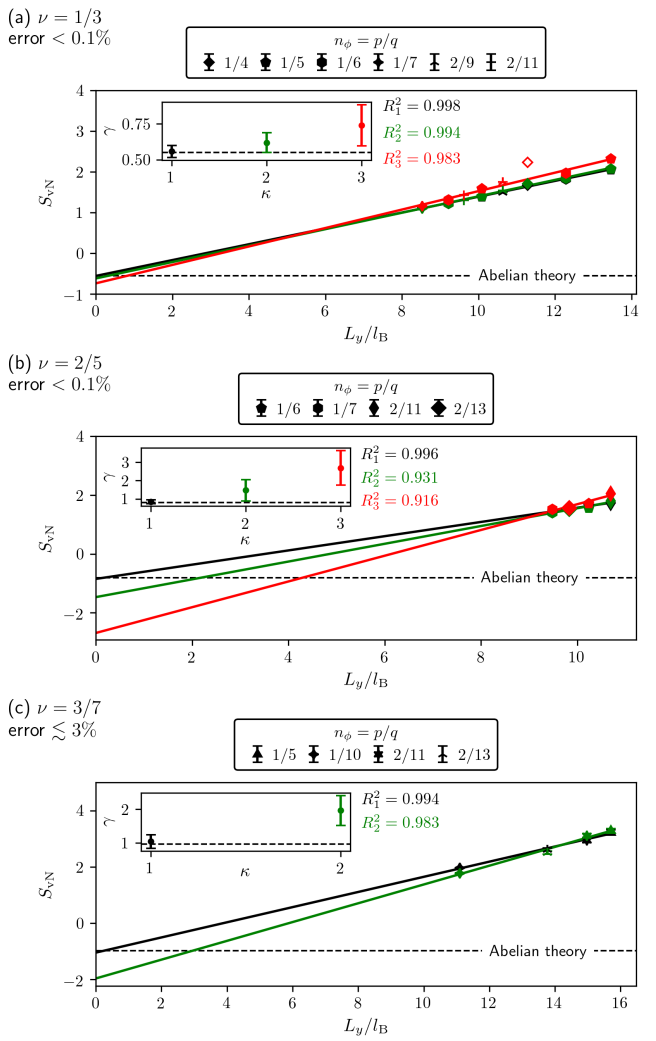


FIG. 3. Tuning the interaction range for the area law plots in Fig. 1. In each case we tune (a, b) the corresponding colored points from Fig. 1.(a, b), and (c) the four colored points from Fig. 1.(c) that are closest to the line of best fit. The data for $\kappa = 1, 2, 3$ is colored in black, green, and red, respectively. The value of the topological entanglement entropy predicted from the Abelian theory, $\gamma = \ln(\sqrt{s})$, is additionally marked with a dashed line. In all cases, we increase the bond dimension of these runs appropriately such that we maintain the same error threshold. Consequently, the maximum bond dimension is $\chi_{\max} = 4000$ for each filling factor. The $n_\phi = 1/4$, $\kappa = 3$ data point at $\nu = 1/3$ filling is marked as an outlier.

$\gamma_{\kappa=2} = 0.619 \pm 0.068$ and finally $\gamma_{\kappa=3} = 0.738 \pm 0.143$. Throughout this procedure, we ensure that the error standards are maintained to be $< 0.1\%$ and the linearity threshold is consistently $R^2 > 0.98$. Although the errors of the topological entanglement entropies are too large to definitively claim an increase overall, the increase from $\kappa = 1 \rightarrow 3$ is statistically significant with respect to the Abelian theory value. Note that the configuration at $n_\phi = 1/4$ with $\kappa = 3$ was excluded as an outlier. Since this configuration has the smallest system size and MUC

dimension (4×1) out of the eight points, it is unsurprising that it exhibits prohibitively large finite-size effects for the case of up to third nearest-neighbor interactions.

In Fig. 3.(b) we present the analogous plot for the $\nu = 2/5$ state. We take the four accepted data points from Fig. 1.(b) and maintain the error threshold to be 0.1%. Again, we observe an increase in topological entanglement entropy as we tune interaction range, except on this occasion the increase is larger and statistically significant. The topological entanglement entropy grows from $\gamma_{\kappa=1} = 0.850 \pm 0.103$ to $\gamma_{\kappa=2} = 1.470 \pm 0.588$ and finally $\gamma_{\kappa=3} = 2.673 \pm 0.935$. Although the errors are too high to comment on the precise values at larger interaction range, the upward trend is clear. Peculiarly, we note that our result at $\kappa = 3$ exceeds the non-Abelian Gaffnian prediction of $\gamma = 1.448^{30}$, which may be attributed to minor finite-size errors, particularly affecting the $n_\phi = 2/11$ data point. Although we went to great lengths to alleviate finite-size effects at $\kappa = 1$, the quality of the configurations is expected to deteriorate as κ is increased. In order to overcome this, the same systematic procedure would have to be applied at $\kappa = 3$, which is beyond the scope of our computational resources.

Finally, we tune the interaction range for the state at $\nu = 3/7$ filling, as shown in Fig. 3.(c). In this case, we take the four accepted data points that are closest to the line of best fit in Fig. 1.(c). We do this in the interests of computational expense, since the configurations for this filling are already challenging to converge, even at $\kappa = 1$. For consistency, we maintain the same error threshold. Following the trend observed for the previous two fillings, the topological entanglement entropy increases with interaction range and once again by a larger margin than before, such that $\gamma_{\kappa=1} = 0.943 \pm 0.102$ and $\gamma_{\kappa=2} = 1.902 \pm 0.573$. We were not able to adequately alleviate numerical and statistical errors at $\kappa = 3$ for the bond dimensions that were accessible to us. However, the $\kappa = 2$ data already shows a tentative agreement with the non-Abelian prediction and a statistically significant increase from $\kappa = 1$.

V. DISCUSSION AND CONCLUSIONS

In this paper, we have investigated the effective Abelian topological order for the $\nu = 1/3$, $2/5$, and $3/7$ FQH states. Having developed an efficient sampling algorithm that accounts for both numerical and statistical errors, we constructed the area law of entanglement for each of these states and extrapolated to read off the topological entanglement entropies. In all cases, we demonstrated that these states exhibit Abelian topological order when interactions are short-range, which is further corroborated by the edge-state counting. As we tune the interaction range for a Coulomb potential, we observe that the topological entanglement entropies increase indicating the onset of non-Abelian topological order, where the rate and magnitude of the increase scales with the

hierarchy level of the FQH state. Interestingly, even the Laughlin filling signals an increase in topological entanglement entropy when the interaction range is sufficiently large.

Determining the topological order hosted by the prominent FQH plateaus is important, not only to reconcile the various theories in the literature but also due to its practical implications. Manifestations of the FQH states discussed in this paper have already been observed experimentally: such as $\nu = 2+2/5$ in a two-dimensional electron gas^{7,40}, and more recently, $\nu = 1+3/7$ in bilayer graphene¹⁵. Furthermore, if the non-Abelian theory holds, these states have the potential to host Fibonacci anyons, which can be used to construct a universal set of gates in a topological quantum computer. Despite this, the hesitation surrounding the precise conditions under which the $\nu = 2/5$ and $3/7$ states are non-Abelian has lasted over a decade.

Initially, attention was focused on the $\nu = 2/5$, since it is the second most prominent Hall plateau and the second state in the fermion hierarchy. Soon after the introduction of the Abelian Jain state¹¹, the corresponding Gaffnian was derived, analogously to the Pfaffian, from a pseudopotential Hamiltonian dictated by a CFT description¹². At the time, the state was predominantly of interest due to its non-unitarity⁴¹, however the competition at $\nu = 2/5$ was quickly realized, where finite-size numerics showed that the entanglement spectrum matches the Jain prediction³⁷, and an unusual change in character of the $\nu = 2/5$ excitations was demonstrated⁴². At the same time independent claims were being made that non-Abelian order is favored at this filling⁴³. After several numerical studies characterizing non-Abelian order from clustering Hamiltonians^{44,45}, as well as two-body interactions²² with short²³ and long²⁴ range, the ability to analyze such states greatly improved. As a result of these technical advancements, the latest investigations into the nature of the $\nu = 2/5$ state are currently by Estienne et al.³⁰, who observed the Abelian value for the topological entanglement entropy based on ground-state wavefunctions, and Yang et al.¹, who offered an explanation based on the local exclusion conditions. Most recently, the $\nu = 3/7$ state has also come under similar numerical scrutiny¹⁵.

Building on this substantial body of work, we confirm the effective Abelian topological order of these states at short interaction range. Since our results are based on many-body simulations of a microscopic Hamiltonian using state-of-the-art computational techniques, this is the most intensive study of these ground states to date. Our results corroborate the hypothesis of Yang et al. who claim that there is an implicit assumption of short-range interactions in the Jain hierarchy, and that it is possible to engineer a long-range interaction that tunes away from this topological order. As mentioned in their paper, the same assumption is also present at $\nu = 3/7$. As for the $\nu = 1/3$ state, it is important to note that the Laughlin ansatz is not the exact ground state for the Coulomb interaction but rather for a much simpler short-range inter-

action⁴⁶. It is therefore unreasonable to expect a priori that the Abelian Laughlin state will persist as the interaction range is increased. It has also been previously noted that such Abelian states may be destabilized in the long-range interaction limit²⁴.

Future studies in this direction could address the increasing rate of non-Abelian order onset at higher hierarchy levels, as well as accurate estimates for the topological entanglement entropy at large κ . Specifically, the precise non-Abelian anyonic statistics have not yet been obtained from a comparable many-body simulation for the $\nu = 2/5$ or $3/7$ states. We hope that this paper will not only highlight the care required when constructing area laws of entanglement but, more broadly, help focus modern research efforts into realizing non-Abelian anyons with realistic two-body interactions in experimentally-relevant systems.

ACKNOWLEDGMENTS

We thank Johannes Hauschild, Apoorv Tiwari, Leon Schoonderwoerd, and Gunnar Möller for useful discussions. Calculations were performed using the **TENPy** Library (version 0.5.0)⁴⁷ and **GNU PARALLEL**⁴⁸. This project was funded by the Swiss National Science Foundation under Grant No. PP00P2_176877.

Appendix A: Numerical method

In an effort to remove arbitrariness from the computation of topological entanglement entropies, we follow a set algorithm for the data collection and analysis. In this appendix, we outline and justify the steps in the procedure. We start with a description of the systematic selection of n_ϕ values in Sec. A 1, we then explain how the entanglement entropy is extrapolated for each configuration in Sec. A 2, and finally show how the line of best fit is constructed for the area law of entanglement in Sec. A 3.

1. Selection of n_ϕ

For a given filling factor, we list all values of the co-prime fraction $n_\phi \equiv p/q$ that satisfy the following constraints:

- $\frac{1}{2\pi} \left(\frac{(L_y/l_B)_{\min}}{L_y} \right)^2 < n_\phi < 0.4$

Due to finite-size effects, we can safely set a lower bound on the $L_y/l_B = \sqrt{2\pi n_\phi} L_y$ values that we produce. From preliminary investigations of the bosonic Laughlin state [Fig. 5.(a)], the simplest FQH state, we found that finite-size effects are sufficiently suppressed at $L_y/l_B \gtrsim 8$. Since finite-size effects for higher-order FQH states require larger

cylinder circumferences to be suppressed, we set at least $(L_y/l_B)_{\min} \equiv 8$. As we proceed up the FQH hierarchy, we can increase this minimum threshold. Furthermore, it has been shown experimentally that Laughlin states require $n_\phi < 0.4$ to be stabilized and that this critical n_ϕ may be lower for higher-order hierarchy states⁴⁹. Hence, we set the upper limit for the flux densities to 0.4.

- $L_y \geq 4$

Since we are interested in the effect of tuning the interaction range across first, second, and third nearest neighbors, we demand that the system size is at least four sites across in the y -direction.

- $4 \leq q \leq 20$

Similar to above, we demand that the system size in the x -direction is also at least four sites across⁵⁰. Furthermore, we set the maximum value to 20 so that we limit the precision of the required flux density values. This makes the results more relevant for experimental set-ups, such as optical flux lattices⁵¹.

- $N_{\min} \geq 2$

We require that the total number of particles in our system ($N = nqL_xL_y$) is an integer greater than or equal to two, for two-body interactions.

- $qL_xL_y \leq N_{s,\max}$

We limit the total size of the MPS unit cell to be less than or equal to $N_{s,\max}$. This restricts the memory cost, which scales linearly with the system size. We adjust the value $N_{s,\max} \sim 100$ depending on computational resources.

- $\Delta_{L_y/l_B} > 0.1$

We require that the separation between L_y/l_B values is greater than 0.1. This is to minimize the susceptibility of the line of best fit to errors in the individual values for the entanglement entropies. It also efficiently provides a greater range of L_y/l_B values to consider. The value of 0.1 was chosen as a compromise between precision and a maximal data set.

Finally, we define a processing cost function $\Gamma(p, q, L_x, L_y) \equiv qL_x e^{L_y + \tilde{n}_\phi}$, where $\tilde{n}_\phi = 20n_\phi$ is the normalized flux density, defined such that the range $1 \leq \tilde{n}_\phi < 8$ is comparable to $6 \lesssim L_y \lesssim 15$. We then sort the configurations in ascending Γ , attempt to converge all of them up to $\chi_{\max} \lesssim 3000$, and use those that are successful.

The processing cost function roughly quantifies how much processing time is needed for a state to converge. It is not the physical processing cost of the iDMRG algorithm itself, which scales (conservatively) as $\sim O(\chi^3 Dd^3 + \chi^2 D^2 d^2)$ for a single bond update, where

D is the MPO bond dimension and d is the single-site Hilbert space dimension. Rather, the processing cost function takes into account the χ required for convergence in a given model. It is well known that the convergence processing cost of the iDMRG algorithm scales linearly with cylinder length and exponentially with cylinder circumference. Moreover, from preliminary investigations of the Laughlin states, we find that a state is more likely to converge with a smaller n_ϕ , showing roughly the same scaling precedence as cylinder circumference.

2. Extrapolation of the entanglement entropy to the $\chi \rightarrow \infty$ limit

Since the final result for the topological entanglement entropy, γ , is highly sensitive to the values of the individual entanglement entropies, S_{vN} , we need to minimize the error in S_{vN} to obtain a representative value for γ . Furthermore, since we are comparing γ between different Hamiltonians, we additionally need to ensure that all S_{vN} are computed to the same accuracy for a fair comparison.

To this end, we study the convergence of S_{vN} with bond dimension χ . An illustrative example for the Laughlin state in the fermionic Hofstadter model is shown in Fig. 4. Figures 4.(a,b) show the convergence of S_{vN} with χ for this system. We can see that as χ is increased, the entropy is approaching a value of 1.43. To quantify this, we note that entropy increases monotonically with bond dimension, as demonstrated in Fig. 4.(c). Hence, the highest- χ value for S_{vN} will be the lower bound of our entropy estimate. Moreover, we know that in the $\chi \rightarrow \infty$ limit, $dS_{vN}/d\chi \rightarrow 0$, which implies that $dS_{vN}/d\chi$ monotonically decreases. Hence the extrapolation of our last estimate of $\Delta S_{vN}/\Delta\chi$ will serve as our upper bound. Since a polynomial fit of all data points is computationally costly, and will have negligible benefits as we reduce the errors, we instead take $\lim_{\chi \rightarrow \infty} S_{vN}$ to be directly in between our lower and upper bounds, as exemplified by the red data point in Fig. 4.(b).

In order to maintain a consistent accuracy among all entanglement entropy values in this manuscript, we continue with the entropy convergence until all $\lim_{\chi \rightarrow \infty} S_{vN}$ estimates have error bars $< 0.1\%$, unless otherwise stated. Consequently, the example system in Fig. 4 is sufficiently converged for $\chi_{\max} = 1100$.

3. Linear regression

For a given area law plot of the entanglement entropy, there can be great variability in the y -intercept of the linear regression depending on which points are considered, as shown in Fig. 5. Moreover, it is known that finite-size effects become significant for small systems, and in the extreme case, the area law even breaks down since $S = \alpha L_y - \gamma + O(e^{-L_y})$. Therefore, there is motivation to carefully reject data with small cylinder circumferences

without biasing the final result for the topological entanglement entropy. To reconcile this issue, we use an algorithm to construct the line of best fit.

For all the data points on the plot, we draw lines of best fit: the first of which considers all of the data, the second rejects the smallest L_y/l_B point, the third rejects the smallest two L_y/l_B points, etc. We continue in this manner until we reach a line that satisfies $R^2 > 0.99$. It is this line that we use for our linear regression. The data is quantifiably linear and so finite-size effects are suppressed, and we take the first such line because it is based on the most points.

Appendix B: Complete data sets

In Fig. 5, we present the complete set of data collected in this project, both systematic and unsystematic. Along with the area law of entanglement in the top panel of each plot, we also present the topological entanglement entropy estimate from including all points with a cylinder circumference $\geq L_y/l_B$ (middle panel), along with the corresponding R^2 values for each of these linear regressions (bottom panel).

In Fig. 5.(a,b) we show data for the bosonic and fermionic Laughlin states. For the bosonic Laughlin state, we computed the entanglement entropy for 76 configurations, 46 of which converged with $< 0.1\%$ error and are shown in Fig. 5.(a). Even with the complete $< 0.1\%$ error data set, we still obtain a clear agreement with the Abelian theory value of $\gamma = \ln(\sqrt{2}) \approx 0.347$. We also note that after the $R^2 = 0.99$ threshold, finite-size effects are suppressed since we maintain $R^2 > 0.99$, and the average topological entanglement entropy agrees with the theory based on all values drawn after this point. This plot also highlights the dramatic effect that a few relatively minor outliers (notably $\{n_\phi = 1/3, L_y = 4\}$ and $\{n_\phi = 2/7, L_y = 6\}$) can have on the topological entanglement entropy estimate and raises concerns of selection bias in unsystematic studies. For the fermionic Laughlin state, we computed the entanglement entropy for 89 configurations, 53 of which converged and are shown in Fig. 5.(b). Overall, we notice similar features as for the bosonic Laughlin state. However, we note that on this occasion the complete $< 0.1\%$ error data set does not agree with the Abelian theory. We emphasize that, as with the bosonic Laughlin state, it is simply coincidence whether or not the complete data set agrees with the theory due to the significant finite-size effects at small cylinder circumference. Once we draw a line through all points above the $R^2 = 0.99$ threshold, we do see a clear agreement. As with the bosonic Laughlin state, $R^2 > 0.99$ is maintained above this threshold, which indicates that finite-size effects have been effectively alleviated. Note also that the $R^2 > 0.99$ threshold occurs at $L_y/l_B = 9.21$, which is larger than the bosonic value $L_y/l_B = 8.12$, as expected.

Motivated by the results from the Laughlin states, we construct corresponding plots for the next filling factors

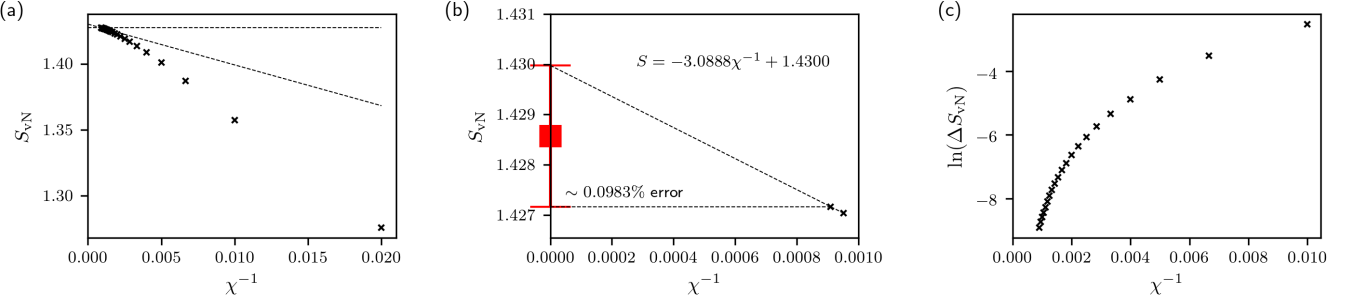


FIG. 4. Extrapolation of the entanglement entropy, S_{vN} , in the $\chi \rightarrow \infty$ limit for the fermionic Hofstadter model at $\nu = 1/3$, with flux density $n_\phi = 1/3$ and cylinder circumference $L_y = 6$. (a) S_{vN} as a function of χ^{-1} , where $\chi \in [50, 100, 150, \dots, 1100]$. (b) A close-up of the last two points shown in (a), including the equation of the straight line through these points, and the $\lim_{\chi \rightarrow \infty}(S_{vN})$ estimate with error bars shown in red. (c) The change in entropy as the bond dimension is incremented, ΔS_{vN} , for the data points in (a).

in the hierarchy: the bosonic $\nu = 2/3$ and fermionic $\nu = 2/5$ states, shown in Fig. 5.(c–e). For the bosonic $\nu = 2/3$ state, we computed the entanglement entropy for 41 configurations, only 5 of which converged, and so we simply show all of the data in Fig. 5.(c). For this filling factor, we are not able to draw any conclusions regarding the topological entanglement entropy. We note incidentally, however, that the value of the topological entanglement entropy for the largest R^2 value gives the closest agreement with the Abelian theory, which indicates potential agreement once finite-size effects are alleviated. For the fermionic $\nu = 2/5$ state we computed 50 entanglement entropies, shown in Fig. 5.(d), and 20 converged to $< 0.1\%$ error, shown in Fig. 5.(e). In this case, when a line is drawn through *all* data points above the R^2_{\max} threshold in Fig. 5.(d), we obtain a close agreement to the Abelian theory value, similar to the result obtained using the $< 0.1\%$ error data. We note however, that the R^2 value does not maintain its large value after the threshold, which indicates that significant fluctuations are still present. In contrast, when we examine exclusively $< 0.1\%$ error data points in Fig. 5.(e), we see that $R^2 > 0.99$ is maintained after the threshold. In keeping with the noted trend, the value at which this occurs, $L_y/l_B = 9.47$, is higher than for the corresponding Laughlin state.

Most ambitiously, we construct an area law plot for the secondary fermionic hierarchy state at $\nu = 3/7$. For this state, we computed the entanglement entropy for 44 configurations, only 12 of which converged to $< 0.1\%$ error. Consequently, we present all of the data in Fig. 5.(f). Given the immense computational effort in obtaining high- L_y/l_B data for the $\nu = 3/7$ state (~ 256 GB of memory and ~ 2 weeks run-time per data point), we analyze this as a stand-alone plot. As demonstrated in Fig. 5.(d), we cannot reliably apply the R^2 threshold analysis, since the error of the data set is not small enough. We also note that for this system both physical (L_y/l_B) and numerical (L_y) finite-size effects are significant. Taking the largest system sizes that we considered, with respect to both

length scales, yields the subset shown in Fig. 1.(c). The extracted data is still significantly noisier than any other data presented in the main text, however the complete data set suggests that these finite-size effects will be alleviated if the cylinder circumference is further increased. Specifically, we again point out that the estimate of the topological entanglement entropy with the largest R^2 value yields the closest agreement to the Abelian theory. This is true for all of the area law plots in our analysis.

Appendix C: Total quantum dimensions

Generalized parafermion FQH states are expected at the filling $\nu = k/(Mk + 2)$, where M even/odd corresponds to bosons/fermions and k is an integer⁵². These states are described by a $SU(2)_k$ Chern-Simons theory in the bulk and the rational CFT $[SU(2)/U(1)]_k \times U(1)_{k(Mk+2)}$ on the edge³⁵. Since the total quantum dimensions for $SU(2)$ or $U(1)$ theories with positive and negative k levels are identical, the total quantum dimension for the coset theory is given as

$$\mathcal{D}_{\text{coset}} = \frac{\sqrt{(|k| + 2)|Mk + 2|}}{2 \sin\left(\frac{\pi}{|k| + 2}\right)}.$$

For the non-Abelian $\nu = 2/5$ state we may set $k = 3$, $M = 1$ to yield $\mathcal{D}_{2/5} = \sqrt{5(\varphi^2 + 1)}$, whereas for the non-Abelian $\nu = 3/7$ state we may set $k = -3$, $M = 3$ to yield $\mathcal{D}_{3/7} = \sqrt{7(\varphi^2 + 1)}$. Note that in both cases this is larger than the Abelian value for the total quantum dimension \sqrt{s} by a factor of $\sqrt{\varphi^2 + 1}$.

Since both the $\nu = 2/5$ and $3/7$ non-Abelian theories have $|k| = 3$, they describe a theory of Fibonacci anyons⁵³. As mentioned in the main text, the total quantum dimension must take the form $\mathcal{D} = \sqrt{\sum_a d_a^2}$, where d_a is the quantum dimension of a quasiparticle of type a . For Abelian anyons $d_a = 1$, whereas for non-Abelian anyons $d_a > 1$ ²⁸. Furthermore, for any $\nu = r/s$ FQH

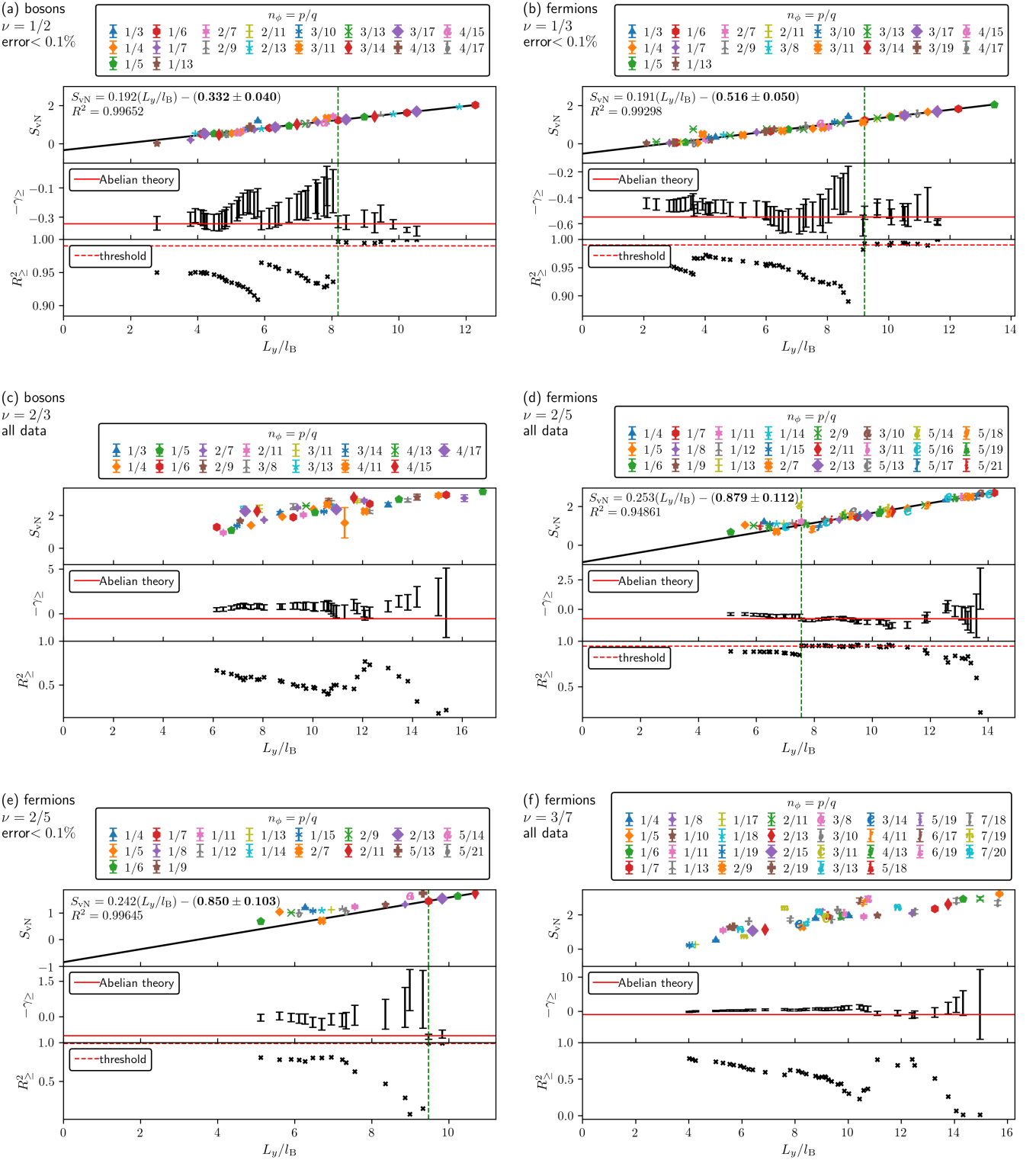


FIG. 5. The complete data sets for the (a) bosonic and (b) fermionic Laughlin (0th hierarchy) states with < 0.1% error; the (c) complete bosonic, (d) complete fermionic, (e) < 0.1% error fermionic 1st hierarchy states; and (f) the fermionic 2nd hierarchy state. (top panels) Von Neumann entanglement entropy, S_{VN} , plotted as a function of cylinder circumference, L_y , in units of magnetic length, $l_B = (2\pi n_\phi)^{-1/2}$. The line of best fit is drawn through the set of points above the smallest L_y/l_B that yields $R^2 > 0.99$ for < 0.1% error data and $R^2 = R_{\max}^2$ otherwise. This cut-off is marked with a green dashed line. (middle panels) The y -intercept of the line of best fit drawn through all points greater than or equal to L_y/l_B , denoted as $-\gamma_>$. The Abelian theory prediction, $\gamma = \ln(\sqrt{s})$, is marked in red. (bottom panels) The square of Pearson's correlation coefficient for the line of best fit drawn through all points greater than or equal to L_y/l_B , denoted as $R^2_>$. The corresponding threshold, either $R^2 = 0.99$ or R_{\max}^2 , is marked with a red dashed line.

state the ground-state degeneracy must be at least s , which confirms the minimum Abelian value for the total quantum dimension \sqrt{s} . In addition to Abelian anyons, a Fibonacci theory also hosts non-Abelian anyons of quan-

tum dimension φ^{54} . Therefore, based on these two arguments alone, the total quantum dimension for a $|k| = 3$ theory must take the form $\mathcal{D}_{|k|=3} = \sqrt{\alpha\varphi^2 + \beta}$, where α, β are positive integers satisfying $\alpha + \beta \geq s$.

¹ B. Yang, Y.-H. Wu, and Z. Papić, *Phys. Rev. B* **100**, 245303 (2019).

² J. M. Leinaas and J. Myrheim, *Il Nuovo Cimento B* (1971-1996) **37**, 1 (1977).

³ F. Wilczek, *Phys. Rev. Lett.* **49**, 957 (1982).

⁴ J. Fröhlich, “Statistics of fields, the yang-baxter equation, and the theory of knots and links,” in *Nonperturbative Quantum Field Theory*, edited by G. ’t Hooft, A. Jaffe, G. Mack, P. K. Mitter, and R. Stora (Springer US, Boston, MA, 1988) pp. 71–100.

⁵ G. Moore and N. Read, *Nuclear Physics B* **360**, 362 (1991).

⁶ X. G. Wen, *Phys. Rev. Lett.* **66**, 802 (1991).

⁷ C. Nayak, S. H. Simon, A. Stern, M. Freedman, and S. Das Sarma, *Rev. Mod. Phys.* **80**, 1083 (2008).

⁸ S. D. Sarma, M. Freedman, and C. Nayak, *npj Quantum Information* **1**, 15001 (2015).

⁹ R. B. Laughlin, *Phys. Rev. Lett.* **50**, 1395 (1983).

¹⁰ F. D. M. Haldane, *Phys. Rev. Lett.* **51**, 605 (1983).

¹¹ J. K. Jain, *Phys. Rev. Lett.* **63**, 199 (1989).

¹² S. H. Simon, E. H. Rezayi, N. R. Cooper, and I. Berdnikov, *Phys. Rev. B* **75**, 075317 (2007).

¹³ D. Green, arXiv e-prints , cond-mat/0202455 (2002), [arXiv:cond-mat/0202455 \[cond-mat.str-el\]](https://arxiv.org/abs/cond-mat/0202455).

¹⁴ N. Read and D. Green, *Phys. Rev. B* **61**, 10267 (2000).

¹⁵ W. N. Faugno, J. K. Jain, and A. C. Balram, arXiv e-prints , arXiv:2006.00238 (2020), [arXiv:2006.00238 \[cond-mat.str-el\]](https://arxiv.org/abs/2006.00238).

¹⁶ D. R. Hofstadter, *Phys. Rev. B* **14**, 2239 (1976).

¹⁷ Y. Aharonov and D. Bohm, *Phys. Rev.* **115**, 485 (1959).

¹⁸ R. Peierls, *Zeitschrift für Physik* **80**, 763 (1933).

¹⁹ J. Zak, *Phys. Rev.* **134**, A1602 (1964).

²⁰ M. Y. Azbel, *JETP* **19**, 634 (1964).

²¹ B. Andrews and G. Möller, *Phys. Rev. B* **97**, 035159 (2018).

²² B. Kuśmierz and A. Wójs, *Phys. Rev. B* **97**, 245125 (2018).

²³ Z. Liu, D. L. Kovrizhin, and E. J. Bergholtz, *Phys. Rev. B* **88**, 081106(R) (2013).

²⁴ Z. Liu, E. J. Bergholtz, and E. Kapit, *Phys. Rev. B* **88**, 205101 (2013).

²⁵ S. R. White, *Phys. Rev. Lett.* **69**, 2863 (1992).

²⁶ U. Schollwöck, *Annals of Physics* **326**, 96 (2011), january 2011 Special Issue.

²⁷ L. Cincio and G. Vidal, *Phys. Rev. Lett.* **110**, 067208 (2013).

²⁸ A. Kitaev and J. Preskill, *Phys. Rev. Lett.* **96**, 110404 (2006), [arXiv:hep-th/0510092 \[hep-th\]](https://arxiv.org/abs/hep-th/0510092).

²⁹ M. Levin and X.-G. Wen, *Phys. Rev. Lett.* **96**, 110405 (2006).

³⁰ B. Estienne, N. Regnault, and B. A. Bernevig, *Phys. Rev. Lett.* **114**, 186801 (2015).

³¹ A. G. Grushin, J. Motruk, M. P. Zaletel, and F. Pollmann, *Phys. Rev. B* **91**, 035136 (2015).

³² L. Schoonderwoerd, F. Pollmann, and G. Möller, arXiv e-prints , arXiv:1908.00988 (2019), [arXiv:1908.00988 \[cond-mat.str-el\]](https://arxiv.org/abs/1908.00988).

³³ B. Andrews and A. Soluyanov, *Phys. Rev. B* **101**, 235312 (2020).

³⁴ The difficulty in computing higher filling fractions in the FQH hierarchy is not only due to the more restrictive geometry constraints but also due to the increased sensitivity of these states with respect to interaction strength and gap-to-width ratio.

³⁵ S. Dong, E. Fradkin, R. G. Leigh, and S. Nowling, *Journal of High Energy Physics* **2008**, 016 (2008).

³⁶ X.-G. Wen, *International Journal of Modern Physics B* **06**, 1711 (1992), <https://doi.org/10.1142/S0217979292000840>.

³⁷ N. Regnault, B. A. Bernevig, and F. D. M. Haldane, *Phys. Rev. Lett.* **103**, 016801 (2009).

³⁸ B. A. Bernevig and F. D. M. Haldane, *Phys. Rev. Lett.* **101**, 246806 (2008).

³⁹ S. Pu, Y.-H. Wu, and J. K. Jain, *Phys. Rev. B* **96**, 195302 (2017).

⁴⁰ J. S. Xia, W. Pan, C. L. Vicente, E. D. Adams, N. S. Sullivan, H. L. Stormer, D. C. Tsui, L. N. Pfeiffer, K. W. Baldwin, and K. W. West, *Phys. Rev. Lett.* **93**, 176809 (2004).

⁴¹ T. Jolicoeur, T. Mizusaki, and P. Lecheminant, *Phys. Rev. B* **90**, 075116 (2014).

⁴² C. Töke and J. K. Jain, *Phys. Rev. B* **80**, 205301 (2009).

⁴³ M. C. Diamantini and C. A. Trugenberger, *Journal of Physics A: Mathematical and Theoretical* **44**, 115001 (2011).

⁴⁴ Y.-F. Wang, H. Yao, Z.-C. Gu, C.-D. Gong, and D. N. Sheng, *Phys. Rev. Lett.* **108**, 126805 (2012).

⁴⁵ Y.-L. Wu, B. A. Bernevig, and N. Regnault, *Phys. Rev. B* **85**, 075116 (2012).

⁴⁶ S. A. Trugman and S. Kivelson, *Phys. Rev. B* **31**, 5280 (1985).

⁴⁷ J. Hauschild and F. Pollmann, *SciPost Phys. Lect. Notes* , 5 (2018), code available from <https://github.com/tenpy/tenpy>, [arXiv:1805.00055](https://arxiv.org/abs/1805.00055).

⁴⁸ O. Tange, *:login: The USENIX Magazine* **36**, 42 (2011).

⁴⁹ M. Hafezi, A. S. Sørensen, E. Demler, and M. D. Lukin, *Phys. Rev. A* **76**, 023613 (2007).

⁵⁰ These conditions on L_y and q do not guarantee that a system will be large enough to sufficiently suppress finite-size effects, as exemplified by the outlier in Fig. 3.(a).

⁵¹ D. Jaksch and P. Zoller, *New Journal of Physics* **5**, 56 (2003).

⁵² N. Read and E. Rezayi, *Phys. Rev. B* **59**, 8084 (1999).

⁵³ J. Slingerland and F. Bais, *Nuclear Physics B* **612**, 229 (2001).

⁵⁴ C. Gils, S. Trebst, A. Kitaev, A. W. W. Ludwig, M. Troyer, and Z. Wang, *Nature Physics* **5**, 834 (2009).